

The Oceanic Excitation Hypothesis for the Continuous Oscillations of the Earth

T. Tanimoto

Institute for Crustal Studies and Department of Geological Sciences,

University of California, Santa Barbara, California 93106

SUMMARY

The continuous oscillations of the Earth are observed for frequencies between 2 and 7 mHz at almost every seismically-quiet site in the world. These oscillations ride on a broad noise peak which spans in the frequency band from 3 to 15 mHz and reaches its maximum at 7-9 mHz. We propose an oceanic excitation hypothesis which explains both the modal oscillations and the broad noise peak, specifically by the action of oceanic infragravity waves on the solid Earth. Using the estimated amplitudes of oceanic infragravity waves from observation, although they are limited in number at the moment, we show that there is sufficient energy in these waves to excite observed seismic signals; for a given time window, contribution from a small area which may be as small as 100 km x 100 km is all that is required to explain seismic observation. The advantage of this oceanic mechanism over the previously-proposed atmospheric mechanism is in the simultaneous explanation of the above two features in seismograms, whereas the atmospheric hypothesis has only explained the modal oscillations. The oceanic mechanism naturally explains the predominant six-months periodicity by semi-hemispheric ocean-wave activities in the northern and southern hemispheres, showing a good match between seismic data and satellite ocean-wave data both in amplitude and phase of seasonal variations. Our Earth seems to be

filled with ubiquitous propagating Rayleigh waves, generated directly by oceanic infragravity waves, for the frequency band 3-15 mHz.

Key words: Normal modes, eigentheory, oceans, seismic noise

1 INTRODUCTION

By analysing high-quality global broadband seismic instruments, Peterson (1993) documented basic characteristics of seismic noise and created a very useful reference model. Fig. 1 shows his model, called NLNM, for frequencies between 1 mHz (millihertz) and 10 Hz. The arrow in the figure points to the frequency band of the subject of this paper. As is well known, this frequency band is sandwiched between two major seismic noise frequency bands, one for frequencies below 2-3 mHz and the other at about 50-200 mHz (peak at a period about 7 seconds). The causes of these peaks are basically known; the former is caused by the atmospheric effects (Warburton and Goodkind, 1977; Zürn and Widmer, 1995) and the latter by ocean waves and is often referred to as microseisms (Longuet-Higgins, 1950; Gutenberg, 1950; Hasselman, 1963).

In this paper, we focus on the cause of the small peak indicated by the arrow in Fig. 1. This peak is commonly found in vertical component seismograms at seismically-quiet sites in the world. It is not found in horizontal components, probably because of the higher noise level in them. Close examination of spectra in this frequency band brings out additional features, not noted at the time of Peterson's (1993) study; an example is given in Fig. 2, which shows an average acceleration power spectral density (acceleration PSD) from 11 globally distributed stations. Peterson's (1993) model (NLNM) is shown by solid circles in the top panel for comparison. The bottom panel gives an expanded view to a small box in the top panel and shows that there are many continuously excited modes within the frequency band. Close match between modal peaks and the eigenfrequencies of an earth model PREM (Dziewonski and Anderson, 1981) unambiguously shows that all peaks are fundamental spheroidal modes. These modes were reported in 1998 for the first time (Nawa et al., 1998; Suda et al., 1998; Tanimoto et al., 1998; Kobayashi and Nishida, 1998) and further analyses on the characterization of modes and on the mechanism of excitation followed since then (Tanimoto and Um, 1999; Nishida et al., 2000; Roult and Crawford, 2000; Ekström, 2001; Tanimoto, 2001; Fukao et al., 2002).

This example in Fig. 2 is shown to emphasize that there are two distinct features in the seismic spectra that require explanation: (1) the continuous oscillations (individual modal

peaks) and (2) the broad noise peak between 3 and 15 mHz (with the maximum at 7-9 mHz). The major purpose of this paper is to present a case that the interaction between the ocean and the solid Earth, through the oceanic infragravity waves, can explain both phenomena. Previously, the cause of the continuous oscillations was argued to be by the atmosphere-solid Earth interaction (Tanimoto and Um, 1999; Fukao et al., 2002). However, the arguments in the atmospheric hypotheses have basically ignored the broad noise peak and only addressed the cause for the modal peaks; in fact, the broad noise peak was regarded as a background noise and was removed when modal amplitudes were estimated. The oceanic hypothesis in this paper can explain both features simultaneously and thus seems more preferable.

It may be worth noting, however, that the atmosphere is always the ultimate source of energy, because ocean waves are excited by the atmosphere-ocean interactions. The main point of our argument is that this energy must be filtered through an ocean process in order to generate the observed seismic features between 3 and 15 mHz.

After submission of the original manuscript, it came to our attention that Rhie and Romanowicz (2004) performed an observational study, using two arrays of seismic networks, to locate the source of the continuous oscillations. Their results indicate that the sources are related to hemispheric mid-latitude ocean-wave behaviors. This is generally consistent with our proposed mechanism, especially in explaining the modal amplitude maximums in January and July. While their study presents good observational evidence, this study presents theoretical evidence that favors the oceanic excitation hypothesis, specifically the simultaneous explanation of the amplitude behaviors of the continuous oscillations and the origin of the broad amplitude highs between 3 and 15 mHz.

In the next section, we will summarize some observational features in the oceanic infragravity waves. We then derive a theoretical normal-mode formula in section 3 and discuss some observational constraints, numerical results and their implications in section 4.

2 OCEANIC INFRAGRAVITY WAVE

It was shown in the last decade that the long-wavelength oceanic gravity waves, known as infragravity waves, are a ubiquitous phenomenon in the oceans (Webb et al., 1991; Webb, 1998). These oceanic (surface) waves produce significant pressure fluctuations at sea bottom at low frequencies because of deep penetration of energy. This is related to the fact that the eigenfunctions of these oceanic surface modes start to touch the ocean bottom at low frequencies; Fig. 3 shows three cases of oceanic surface waves at frequencies 3.3, 10 and 20 mHz, with vertical (U) and horizontal eigenfunctions (V) computed for an Earth model PREM

(Dziewonski and Anderson, 1981). In this model, the upper 3 km is the ocean. This figure shows clearly that the mode at 20 mHz is almost entirely confined to an oceanic layer and thus does not cause much pressure fluctuation at ocean bottom. But ocean waves at 10 mHz or below this frequency have significant amplitudes at ocean bottom with associated pressure changes. These are the (linear) oceanic infragravity waves.

If the infragravity waves are ubiquitous in the ocean, it means that the ocean is constantly exerting fluctuating pressure on the solid Earth. In the model we propose below, we assume that the ocean is filled with propagating infragravity waves. The oceanic layer is regarded as an external forcing source which exerts (stochastic) pressure on the solid Earth.

For an inviscid layer with a rigid bottom boundary, pressure at the surface (P_0) is related to pressure at the bottom by $P_0/\cosh(kH)$ where k is the wavenumber of infragravity waves and H is the ocean depth (e.g., Phillips, 1977). The dispersion relation of oceanic gravity waves is given by $\omega^2 = gk \cdot \tanh(kH)$ where ω is the angular frequency and g is the gravitational acceleration. This formula is derived under the rigid sea-bottom boundary condition and thus, strictly speaking, is incorrect for the case of elastic boundary condition at the sea bottom. But comparisons of the analytical rigid sea-bottom eigenfunctions to the elastic eigenfunctions (Fig. 3) show excellent agreement; differences are about one percent or less and do not affect our discussions in this paper. Therefore, we will adopt the form $P_0/\cosh(kH)$ for sea-bottom pressure and use it in theory for the source of excitation.

For numerical evaluation of normal-mode formulas in the next section, it is necessary to use an estimate for P_0 , or more precisely its power spectral density $\langle P_0^2 \rangle$ (hereafter pressure PSD). In order to see its size and how it changes with geographic locations, we have collected published data and made our own estimates. Fig. 4 shows an example from a location near Japan (Watada et al., 2001); the solid line corresponds to the case $\langle P_0^2 \rangle = 3 \times 10^3$ (Pa^2/Hz) and the two dash lines indicate $\langle P_0^2 \rangle = 10^4$ and 10^3 (Pa^2/Hz), respectively. Interestingly, Watada et al. (2001) also reported atmospheric pressure changes from a barograph near this station (at ocean surface) and its pressure spectral density which is plotted by open circles; it is clear that the atmospheric effects are lower by an order of magnitude for the frequency range of our interest. This is an extremely interesting observation which lends support to the oceanic excitation mechanism, but we do not go into details in this paper.

Results from two other locations are shown in Fig. 5 and 6, after Webb et al. (1991) and Webb (1998). Fig. 5 (East Pacific Rise) shows three lines, 3×10^5 (dashed), 10^5 (solid), and 3×10^4 (dashed) and Fig. 6 shows 300 (dashed), 100 (solid) and 30 (dashed). A summary of the estimates, including observations from other locations, is given in Table 1. The result for

the last location in this table, an IRIS station H2O, is based on our analysis of data from 1999 to 2002.

While the number of data is limited, we can make some inferences based on these estimates of $\langle P_0^2 \rangle$; first of all, a large pressure PSD is of the order of 10^4 - 10^5 (Pa^2/Hz). In the next section, we will use 10^4 for numerical evaluation of theoretical formulas. Also there is a hint that wave amplitudes are small in deep oceans and the infragravity waves are more commonly found in shallow oceans, perhaps confined to regions with depths less than 4000 m.

The latter inference is consistent with the physics of ocean wave generation and propagation; the generation of ocean waves, obviously by the atmosphere-ocean interactions, become efficient when the atmospheric wind velocity becomes close to the phase velocity of ocean waves. Velocity of long-period ocean waves are, roughly speaking \sqrt{gH} , thus becoming small at shallow depths. \sqrt{gH} is about 220 (m/s) for 5 km ocean and 90 (m/s) for 1 km ocean. Typical wind velocities rarely exceed a few tens of meters, but at shallow oceans this can become quite close. Therefore, the generation of the oceanic infragravity waves is likely to be efficient in shallow oceans.

Once generated, these waves tend to be confined to shallow oceans because of refraction due to velocity gradients; this is because waves that propagate toward deeper ocean tend to be refracted back due to velocity increase, implied in \sqrt{gH} . In essence, infragravity waves tend to be trapped to shallow regions (Okiihiro et al., 1992). Therefore, the combination of generation in shallow oceans and the trapping mechanism by refraction leads naturally to more common observation of the infragravity waves in shallow oceans. These waves may reach oceans with depth about 4000 m, however, as the result for the Atlantic ocean in Table 1 suggests. Although these points are not proven by the data, they are certainly consistent with the results in Table 1.

3 NORMAL MODE FORMULA

In the proposed mechanism, the source of excitation is pressure variations at sea bottom generated by the oceanic infragravity waves. Since the infragravity waves can be generated over multiple areas simultaneously, pressure variations are treated here as stochastic quantities both in space and time. Analysis of normal mode excitation in such a case has been published by Tanimoto (1999) and Fukao et al. (2002) for the atmospheric excitation of normal modes. Formulas developed in these papers can be modified for the current oceanic excitation problem.

If the pressure variation on the surface is denoted by P , the vertical displacement in time at colatitude θ and longitude ϕ , $u_r(\theta, \phi, t)$, is given by

$$u_r(\theta, \phi, t) = \sum_n \sum_l \frac{U_{nl}^2(R)}{\omega_l} \sum_m a_l^m(t) Y_l^m(\theta, \phi), \quad (1)$$

where the summations are over the overtone number n , the angular degree l and the azimuthal number m , $U_{nl}(R)$ is the vertical eigenfunction evaluated at the surface (at radius R), ω_l is the angular eigenfrequency of normal modes, Y_l^m is the spherical harmonic and a_l^m is defined by

$$a_l^m(t) = - \int_{-\infty}^t dt' e^{-\frac{\omega_l(t-t')}{2Q_l}} \sin \omega_l(t-t') \int_A d\Omega' P(\theta', \phi', t') Y_l^m(\theta', \phi'). \quad (2)$$

Forming the autocorrelation function for $u_r(t)$ and introducing the pressure power cross-spectral density function $S_p(\theta', \phi', \theta'', \phi''; \omega)$ between two locations (θ', ϕ') and (θ'', ϕ'') , we can write the power spectral density for acceleration by

$$S(\theta, \phi, \omega) = \sum_{n, n'} \sum_{l, l'} \gamma_l \gamma_{l'} \frac{U_{nl}^2(R) U_{n'l'}^2(R)}{F_l(\omega) F_{l'}(\omega)^*} \int_A d\Omega' \int_A d\Omega'' P_l(\cos \Theta') P_{l'}(\cos \Theta'') S_p(\theta', \phi', \theta'', \phi''; \omega) \quad (3)$$

where $\gamma_l = (2l + 1)/4\pi$,

$$F_{nl}(\omega) = \left(\frac{\omega_{nl}}{\omega}\right)^2 - \left(1 + i \frac{\omega_{nl}}{2Q_{nl}\omega}\right)^2, \quad (4)$$

Q_{nl} is the modal attenuation parameter, and Θ' is the distance between (θ, ϕ) and (θ', ϕ') and Θ'' is the distance between (θ, ϕ) and (θ'', ϕ'') . Surface integral variables in (3) are $d\Omega' = R^2 \sin \theta' d\theta' d\phi'$ and $d\Omega'' = R^2 \sin \theta'' d\theta'' d\phi''$. While the above formulation incorporates contributions from overtones, the main contribution to the observed spectra arises from fundamental modes; therefore, we will drop overtones from the summations hereafter and write ω_l , F_l and Q_l instead of ω_{nl} , F_{nl} and Q_{nl} .

We proceed to make two assumptions; (i) the correlation length in S_p is the same as the wavelength λ of the infragravity waves (typically ~ 10 km), and (ii) sea-bottom pressure PSD can be written by

$$S_p(\theta, \phi; \omega) = \frac{\langle P_0^2 \rangle}{\cosh^2\{kH(\theta, \phi)\}} \quad (5)$$

where $H(\theta, \phi)$ is the ocean depth at (θ, ϕ) . Under these assumptions, we can approximate (3) by

$$S(\theta, \phi, \omega) = \sum_{l, l'} \gamma_l \gamma_{l'} \frac{U_l^2(R) U_{l'}^2(R)}{F_l(\omega) F_{l'}(\omega)^*} \pi \lambda^2 \int_A d\Omega' P_l(\cos \Theta') P_{l'}(\cos \Theta') \frac{\langle P_0^2 \rangle}{\cosh^2(kH)} \quad (6)$$

because λ is relatively small in comparison to the wavelengths of normal modes. Here, Θ' is the distance from a particular oceanic location to a seismic station. Integration should be extended to all relevant oceanic area.

4 NUMERICAL EVALUATION

For numerical evaluation of (6), the following procedures were adopted; the normal-mode eigenfunctions that are needed were those of PREM. The surface pressure variations by oceanic infragravity waves, $\langle P_0^2 \rangle$, was assumed to be 10^4 (Pa^2/Hz). Ocean depth variations were included in the integration, for which we used averaged ocean depths over 1 degree by 1 degree.

Since we will compare theoretical results to the observed acceleration PSD in Fig. 2, we evaluated (6) at 11 locations that led to the results in Fig. 2 and took the average. For computation of theoretical PSD at each (θ, ϕ) , we proceeded as follows; first, we picked an angular frequency ω . For each integration over a small oceanic area, the average ocean depth in the area was derived from the ocean bathymetric data and, using $\omega^2 = gk \tanh kH$, the wavenumber was determined for this ω . Then, the summations over the two angular degrees, l and l' , were performed over this small area. The maximum angular degree for these summations was $l = l' = 320$. The same procedure was repeated for all relevant regions and then the whole process was repeated for all frequencies between 3 and 15 mHz.

A straightforward integration of (6) for all regions with depth less than 4000 m led to an estimate of $S(\theta, \phi, \omega)$ that is many orders of magnitude larger than the seismically observed amplitudes in Fig. 2. The clear implication was that the contribution must be coming from a smaller region. After some trial and error, we found that only an area 100 km x 100 km is needed to produce seismically observed amplitudes. As noted above, this estimate for the size of an area is under the assumption $\langle P_0^2 \rangle = 10^4$; if we assumed $\langle P_0^2 \rangle = 10^3$ instead of 10^4 , the area must be ten times larger in order to produce the same amplitudes, making it approximately 300 km x 300 km. Such a trade-off between the assumed $\langle P_0^2 \rangle$ and the 'required' area to match the observed values is obvious from (6) but it is important to note that the area remains relatively small. Observed values for $\langle P_0^2 \rangle$ ($10^3 - 10^4$) place some important bounds on this point.

In order to examine the differences due to geographic locations, we experimented by putting the sources at eight different locations, shown in Fig. 7. Locations 1-3 are in the northern hemisphere and 4-8 are in the southern hemisphere. Each location was assumed to have an area 100 km x 100 km with $\langle P_0^2 \rangle = 10^4$. Results are shown in Fig. 8, with ID numbers (1-8) and ocean depths given at top-right corners. Computed acceleration PSDs in Fig. 8 are similar to the one in Fig. 2, matching the maximum amplitude (4×10^{-19}) approximately. Two main features in the observation, the existence of the broad noise peak between 3 and 15 mHz and the modal peaks on the lower frequency side of this peak, are reproduced in most cases in Fig. 8. However, some differences are found at higher frequencies,

especially above 10 mHz; for example, the result at location 5 shows a much flatter high-frequency asymptote than the observation. This behavior turned out to be closely related to the differences in ocean depths. In order to show this point, we calculated the acceleration PSDs at two locations, in the neighborhood of the location 5, whose depths are 497 m and 1955 m. These two locations are shifted to the west by 10 and 20 degrees from the location 5. Because we compute PSDs at globally distributed 11 stations and take their average, the main difference among them is the ocean depth. Fig. 9 compares these three cases and shows that the high-frequency asymptotic behaviors at frequencies above 10 mHz are clearly different, making amplitudes lower with increasing ocean depth. Among them, the best match with the observed spectra in Fig. 2 is achieved by the source at depth 1955 m.

While this depth about 2000 m is best for a source near the location 5, it does not universally provide the best fit to the observation, however. The goodness of fit seems to change greatly with geographic locations too. For example, three cases involving the northern hemisphere sources (1-3) are at depths over 3000 m, but seem to provide higher frequency asymptotes that generally match the data in Fig. 2; if we chose a shallower depth region in the northern hemisphere, acceleration PSDs above 10 mHz become too large, compared to the observation. Thus, while a depth of about 2000 m gives a good fit for locations near 5, a depth of about 3000 m provides a better fit for sources in the northern hemisphere. Again, unfortunately, this seems to be a non-unique situation. It may suggest that the analysis of data in a form of acceleration PSD (Fig. 2) may be insufficient for resolving the source locations and depths simultaneously.

We noted that there are some distinct differences in spectral shape, if different (shear) Q models were used. Fig. 10 compares acceleration PSDs for three different Q models, one using half the size of PREM (top), the second with PREM (middle) and the third with twice the size of PREM (bottom). There are some differences in absolute amplitudes in Fig. 10. But the main differences among them are in spectral shape, especially in how individual modal peaks emerge out of the background broad noise; the general trend seems to be that the higher the Q values, the more distinct individual modal peaks become. Note that the bottom spectrum shows modal peaks distinctly all the way up to 15 mHz. Clearly, the observed acceleration PSD in Fig. 2 does not display individual modal peaks above 10 mHz, and thus the third case (twice the PREM values) does not match the data. Overall, the data seem to be consistent with a Q model somewhat smaller than the PREM model, although the observed spectral characteristics change to some extent, depending on which stations are used for averaging.

The attenuation alone may not be the only reason for the lack of individual peaks above

10 mHz. Lateral heterogeneity can also help diminish the modal peaks because, as Rayleigh waves circle around the Earth, constructive interference of circling Rayleigh waves will be lost by the complex wave propagation effects (scattering) in the heterogeneous Earth structure. Therefore, we believe the two mechanisms, the attenuation effects and the scattering effects in a heterogeneous Earth, may be contributing to the lack of individual peaks above 10 mHz.

While further clarification of relative importance of these two mechanisms may be interesting, we believe the following recognition is far more important; that is, the reason that individual modal peaks are not seen on the higher frequency side of the broad noise peak (7-9 mHz) is not because spheroidal modes are not excited; they are not seen because of the attenuation effects and the lateral heterogeneity effects. The broad noise peak itself is actually the manifestation of spheroidal-mode energy and this spheroidal-mode energy exists from 3 mHz all the way up to 15 mHz. In other words, the whole signal in this frequency band (3-15 mHz) consists of Rayleigh waves, observed everywhere on the surface of the Earth all the time. The individually observed modal oscillations are only a part of it. Our Earth is filled with these ubiquitous propagating Rayleigh waves in this frequency band.

5 SEASONAL VARIATIONS AND CORRELATION WITH SWH

Seasonal variations in the continuous oscillations, especially the dominant six-months periodicity, were reported by Tanimoto and Um (1999) and Ekström (2001). Here we show evidence of correlation between the six-months variations in seismic data and those in oceanic data; oceanic data are Significant Wave Height (SWH) from satellite data (TOPEX/POSEIDON) for the period 1997-2002.

Predominance of six-months periodicity in seismic data was confirmed in the following way in our approach; we computed seismic spectra every day (24-hour time series) and defined an average modal amplitude by taking the average of spectral amplitudes at eigenfrequencies of 21 spheroidal modes (${}_0S_{20}$ - ${}_0S_{40}$) using the PREM eigenfrequencies. Solid circles in the top panel of Fig. 11 indicate the frequencies we chose. We determine the average amplitude for each day by this procedure. We also make the noise estimates by taking the average of amplitudes at halfway between fundamental spheroidal modes. Open circles in the same figure indicate the results. The plot of such data between 1990 and 1996 (bottom panel, Fig. 11) shows an accumulation of data points near the bottom of this figure, making the bell-shaped distributions in the statistics. The fact that solid circles are systematically higher than open circles is caused by the continuous oscillations. The data within the bell-shaped distributions are the selected data that are not likely to be contaminated by earthquake signals and are

used for further analysis. Data contaminated by local or teleseismic earthquakes have higher amplitudes as some scattered points in the upper part of this figure.

We apply the Fourier analysis to selected data points; because the days that are contaminated by earthquakes are eliminated from the data set, the time series are necessarily sampled at irregular intervals. We thus apply a technique that can handle irregularly sampled time series. Among many potential approaches, we adopted the Lomb-Scargle method (e.g. Press et al., 1986), which is a simple extension of the periodogram approach. Examples of spectra from three stations are shown in Fig. 12, which show that the dominant peaks are at 2 cycles/year or at a period of six months. This feature is commonly found at many other stations.

In the Lomb-Scargle method, phase can also be derived. Using the phase at 2 cycles/year, we plotted the time series from nine stations in Fig. 13. These are monochromatic time series but all data, including the two from the southern hemisphere, are shown to change in phase; two peaks occur within a year, one in December/January/February and the other in June/July/August. Amplitudes of these seasonal variations vary but they are about 4-6 percent.

Satellite data display high ocean-wave amplitudes in the northern hemisphere in December/January/February and in the southern hemisphere in June/July/August, both occurring due to high ocean-wave activities at mid-latitudes between 30 and 60 degrees. An example from 2002 is shown in Fig. 14, which shows high amplitudes in January and in July. In order to quantify this behavior, the integrated power (integration of the square of SWH) for both mid-latitude bands (between 30 and 60 degrees) and for the equatorial region (between south 30 degrees and north 30 degrees) are shown in the top panel of Fig. 15. For each hemisphere, the dominant variation is an annual cycle. But because the peaks in each hemisphere are shifted by six months, the sum of all oceanic regions produces six-months periodicity. The six-months component in the Fourier analysis of integrated power from all oceanic area is shown by a red line in the bottom panel. In this plot, seismic results are shown by blue lines, with solid lines denoting stations in the northern hemisphere and two dashed lines denoting those in the southern hemisphere. Both amplitude and phase seem to match quite well between seismic data and ocean-wave data. There may be a suggestion of slight phase shift, but the size of this shift is within the uncertainties of this analysis.

These results clearly demonstrate that the oceanic excitation hypothesis is entirely consistent with the seismically observed six-months periodicity. We should make a cautionary note on this correlation, however. This is because the peak frequency of ocean-wave data (SWH) is probably caused by waves at about 100 mHz (period 10 seconds) whereas that of the seismic

data is caused by waves at about 10 (3-15) mHz. Strictly speaking, SWH must be shown to correlate with the generation of (much lower frequency) oceanic infragravity waves. We believe it is plausible to assume this correlation but, at the moment, this is not yet proven by data. Scarcity of oceanic infragravity wave data is the critical problem.

6 CONCLUSION

We proposed an oceanic excitation hypothesis for the seismic signal in the frequency band from 3 to 15 mHz. The two main features of observation, the continuous oscillations and the broad noise peak, can be explained by pressure variations caused by the oceanic infragravity waves. An interesting feature is that the contribution from a small area, which may be as small as 100 km x 100 km, is all that is required to explain seismic amplitudes for a typically observed amplitude of oceanic infragravity waves. The advantage of this oceanic mechanism over the previously-proposed atmospheric excitation hypotheses is in the simultaneous explanation of the modal peaks and the broad noise peak by a single mechanism. The reasons that modal peaks are seen only on the lower frequency side of the broad noise peak are attributed to the attenuation effects and the scattering effects (complex propagation effects) in the Earth. Also this oceanic mechanism naturally explains the predominant six-months periodicity due to semi-hemispheric ocean-wave behaviors in summer and winter, matching amplitude and phase of seasonal variations between seismic and ocean-wave data. This feature alone, however, is not the discriminating evidence between the oceanic excitation mechanism and the atmospheric excitation mechanism because the atmosphere also has similar hemispheric activity and thus six-months periodicity.

Although we claim that the proposed oceanic excitation hypothesis should replace the previous atmospheric excitation hypothesis, the original source of energy must be in the atmosphere; after all, the oceanic infragravity waves are generated through the atmosphere-ocean interactions. Our claim is that the original atmospheric energy must be filtered through an ocean process, i.e. through the generation of oceanic infragravity waves, in order to create seismically observable signals in the frequency band 3-15 mHz.

It is also important to note that our Earth is filled with ubiquitous propagating Rayleigh waves in this frequency band, which only becomes apparent in the absence of large earthquakes.

ACKNOWLEDGMENTS

I thank the editor of this paper, Gabi Laske and a reviewer, Göran Ekstrom, for their scrutiny

of the manuscript and Barbara Romanowicz for sending me her preprint with J. Rhie. I also thank Doug ReVelle, Tony Dahlen, Raul Madariaga, and Spahr Webb for various comments on this study. IRIS and GEOSCOPE provided superb service for seismic data retrieval for which I am really grateful. This work was mostly supported by an IGPP grant from Los Alamos National Laboratory and partially by an NSF grant (EAR-0408742) near the end.

REFERENCES

- Dziewonski, A. M. and D. L. Anderson, Preliminary Reference Earth Model, *Phys. Earth Planet. Int.*, *25*, 297-356, 1981.
- Ekström, G., Time domain analysis of Earth's long-period background seismic radiation, *J. Geophys. Res.*, *106*, 26483-26493, 2001.
- Fukao, Y., K. Nishida, N. Suda, K. Nawa, and N. Kobayashi, A theory of the Earth's background free oscillations, *J. Geophys. Res.*, *107*(B9), 2206, 2002.
- Gutenberg, B., Observation and theory of microseisms. *Amer. Meteorol. Soc.*, S. 1303-1311, 1951.
- Hasselmann, K. A., A statistical analysis of the generation of microseisms, *Rev. Geophys.*, *1*, 177-209, 1963.
- Kobayashi, N. and K. Nishida, Continuous excitation of planetary free oscillations by atmospheric disturbances, *Nature*, *395*, 357-360, 1998.
- Longuet-Higgins, M. S., A theory of the origin of microseisms, *Philos. Trans. R. Soc. London, Ser. A*, *243*, 1-35, 1950.
- Nawa, K., N. Suda, Y. Fukao, T. Sato, Y. Aoyama, and K. Shibuya, Incessant excitation of the Earth's free oscillations, *Eath Planets and Space*, *50*, 3-8, 1998.
- Nishida, K., N. Kobayashi, and Y. Fukao, Resonant oscillations between the solid Earth and the atmosphere. *Science*, *287*, 2244-2246.
- Okiihiro, M., R. T. Guza, and R. J. Seymore, Bound infragravity waves, *J. Geophys. Res.*, *97*(C7), 11453-11469, 1992.
- Peterson, J., Observations and modelling of seismic background noise, USGS Open-File Report 93-322, 1993.
- Phillips, O. M., The dynamics of the upper ocean, second edition, Cambridge University Press, 1977.
- Press, W. H., B. P. Flannery, S. A. Teukolsky and W. T. Vetterling, *Numerical Recipes*, Cambridge University Press, 1986.
- Rhie, Junkee and B. Romanowicz, Excitation of earth's incessant free oscillations by Atmosphere-Ocean-Sea-floor coupling, *Nature*, in press, 2004.
- Roult, Genevieve and Wayne Crawford, Analysis of 'background' oscillations and how to improve resolution by subtracting the atmospheric pressure signal, *Phys. Earth Planet. Int.*, *121*, 325-338, 2000.

- Suda, Naoki, K. Nawa, and Y. Fukao, Earth's Background Free Oscillations, *Science*, 279, 2089-2091, 1998.
- Tanimoto, T., Excitation of Normal Modes by Atmospheric Turbulence: Source of Long Period Noise, *Geophys. J. Int.*, 136, 395-402, 1999.
- Tanimoto, T., Continuous Free Oscillations: Atmosphere-Solid Earth Coupling, *Annu. Rev. Earth Planet Sci.*, 29, 563-584, 2001.
- Tanimoto, T., J. Um, Cause of continuous oscillations of the Earth, *J. Geophys. Res.* 104, 28723-28739, 1999.
- Tanimoto, T., J. Um, K. Nishida and N. Kobayashi, Earth's continuous oscillations observed seismically quiet days, *Geophys. Res. Lett.*, 25, 1553-1556, 1998.
- Warburton, R. and J. M. Goodkind, The influence of barometric pressure variations on gravity, *Geophys. J. R. Astr. Soc.*, 48, 281-292, 1977.
- Watada, S., A. Kobayashi, and E. Fujita, Seasonal variations of atmospheric and ocean bottom pressure data in millihertz band, OHP/ION Joint Symposium "Long-Term Observations in the Oceans", p35-37, 2001.
- Webb, S. C., Broadband seismology and noise under the ocean, *Rev. Geophys.*, 36, 105-142, 1998.
- Webb, S. C., X. Zhang, and W. Crawford, Infragravity waves in the deep ocean, *J. Geophys. Res.*, 96, 2723-2736, 1991.
- Zürn, W. and R. Widmer, On noise reduction in vertical seismic records below 2 mHz using local barometric pressure, *Geophys. Res. Lett.*, 22, 3537-3540, 1995.

Table 1. Estimate of $\langle P_0^2 \rangle$ from various regions

Location	Depth (m)	$\langle P_0^2 \rangle$
BOSO ¹	4000	3×10^3
EPR ² (Pacific ³)	3000	10^5
San Diego ⁴	800	10^4
Atlantic ³	4000	10^4
Hebble-a ²	4817	100
Hebble-b ^{2,5}	4817	30
Arctic ³	3000	~ 0
H2O ⁶ (Pacific)	5000	~ 0

Note:

1. Watada et al. (2001)
2. Webb et al. (1991)
3. Webb (1998)
4. Webb and Crawford (1999)
5. When ocean current was strong.
6. IRIS data at H2O station, 1999-2002.

Figure 1. The New Low Noise Model (NLNM) by Peterson (1993). Seismic noise below 3 mHz (red) are dominated by atmospheric effects and noise between 30 mHz and 1 Hz (green) is dominated by ocean effects (microseism). This paper focus on the frequency range between 3 and 15 mHz where Peterson's model show a small noise peak, indicated by the arrow.

Figure 2. Stacked seismic spectra from 11 globally distributed stations between 1 mHz and 15 mHz (top). Expanded view to a small box in the top panel is shown below. The modal peaks of continuous oscillations are shown to match PREM eigenfrequencies of spheroidal fundamental modes. Two features in the top figure is the focus of this paper: the broad noise peak between 3 and 15 mHz with the maximum at 7-9 mHz and the continuous oscillation peaks that emerge mainly on the lower frequency side of this peak.

Figure 3. Eigenfunctions of oceanic surface waves with rigid and elastic sea-bottom boundary conditions. The top 3 km is the ocean and U and V are vertical and horizontal eigenfunctions of spheroidal modes. Dash lines are for rigid sea-bottom solutions (analytical) and solid lines are for elastic sea-bottom boundary conditions (PREM). L is the angular degree, eigenfrequencies are given on their righthand side in mHz, C is phase velocity (km/s) and VG is group velocity (km/s). At 20 mHz, the mode is confined to the ocean. The left two modes (3.3 and 10 mHz) are the oceanic infragravity modes and generate some pressure changes at sea bottom.

Figure 4. Pressure PSD at an ocean bottom station near Japan (off Boso peninsula) by Watada et al. (2001). Solid circles are ocean-bottom pressure PSD. Three lines represent $\langle P_0^2 \rangle = 10^4, 3 \times 10^3, 10^3$ (Pa^2/Hz), respectively from top to bottom. We use 3×10^3 as our best estimate (solid line). Open circles are atmospheric pressure PSD at ocean surface near this station which is shown to be smaller by an order of magnitude.

Figure 5. Ocean bottom PSD data (solid circles) by Webb et al. (1991) near the East Pacific Rise. Our best estimate is given in Table 1. Three lines are for 3×10^5 (dash), 10^5 (solid) and 3×10^4 (Pa^2/Hz).

Figure 6. Ocean bottom PSD data (solid circles) by Webb et al. (1991) near Hebble (Atlantic ocean) when ocean currents are weak. Three lines are for 300 (dash), 100 (solid) and 30 (Pa^2/Hz).

Figure 7. Eight source locations used for computation of the acceleration PSDs in Fig. 8. Three are in the northern hemisphere and five are in the southern hemisphere.

Figure 8. Computed theoretical seismic spectra for each source in Fig. 7. Each case has a source dimension of 100km x 100 km. Two important features in Fig. 2 are reproduced; a broad noise peak that peaks at about 7-9 mHz and the continuous oscillation peaks emerge on the lower frequency side of this peak.

Figure 9. Effects of ocean depth on the acceleration PSD. The shallower the ocean, the flatter the higher frequency asymptotes. These three locations were nearby locations, south of Australia. The middle case is the same with location 5 in Fig. 8.

Figure 10. Effects of attenuation on the shape of PSD. If Q is twice as large as PREM value, modal peaks should also emerge on the higher frequency side of the broad noise peak (bottom). The reason that we only see modes on the lower frequency side is related to the Q values in the Earth.

Figure 11. Stacking of spectral amplitudes were performed by taking the average of modal amplitudes ${}_0S_{20-0}S_{40}$ everyday. These numbers, computed everyday, are distributed like those in the bottom panel. From this figure, we can select data that are not contaminated by earthquakes. Typically, we use the bell-shaped region in the statistics (the bottom-right panel) for further analysis.

Figure 12. Fourier spectra of selected data in Fig. 11. All three stations display the dominant peak at 2 cycles/year or at a period of 6 months.

Figure 13. Using phase determined from the Fourier analysis, the monochromatic time series at 6-months periodicity are plotted. Data from nine stations are plotted including two stations in southern hemisphere. All data are basically in phase, generating two peaks one in December/January/February and the other in June/July/August. Amplitude variations are 4-6 percent.

Figure 14. Significant Wave Height data from TOPEX/POSEIDON data in 2002. There is a high amplitude band at mid-latitude in northern hemisphere in January and another high amplitude band in southern hemisphere in July. Combination of these effects create six-months periodicity.

Figure 15. (TOP) Integrated ocean wave power (square of wave height) for 1997-2002. Red is for the southern hemisphere mid-latitude band (between 30S and 60S), blue is for the northern hemisphere mid-latitude band (between 30N and 60 N) and green is for the region inbetween (from 30S to 30N). (BOTTOM) Integrated ocean wave power for the whole region was Fourier transformed and its six-months component is shown by a red line. It matches with seismic data (blue lines) both in phase and amplitude. Solid blue lines are from seismic stations in the northern hemisphere and dash lines are those in the southern hemisphere.

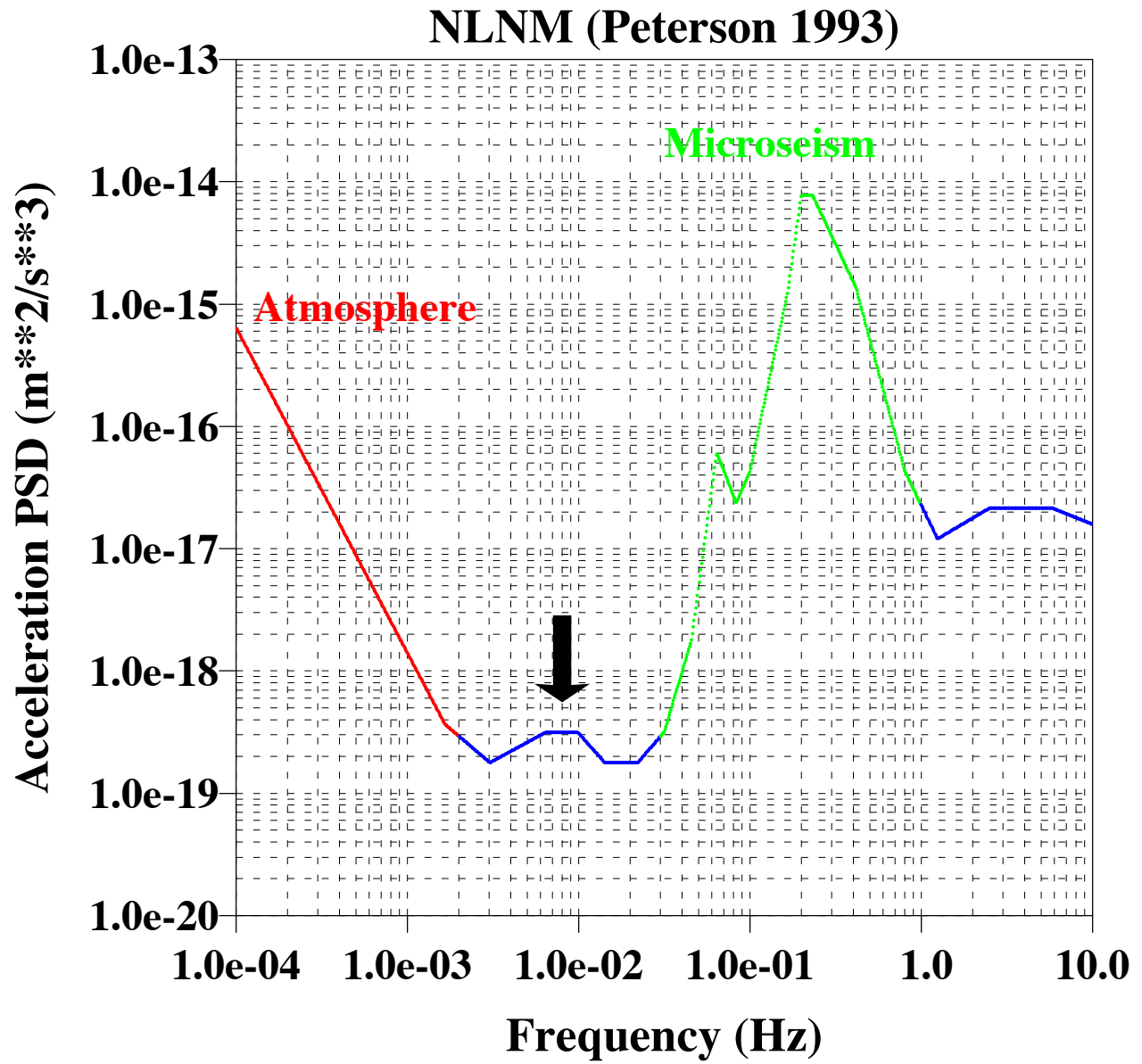


Figure 1

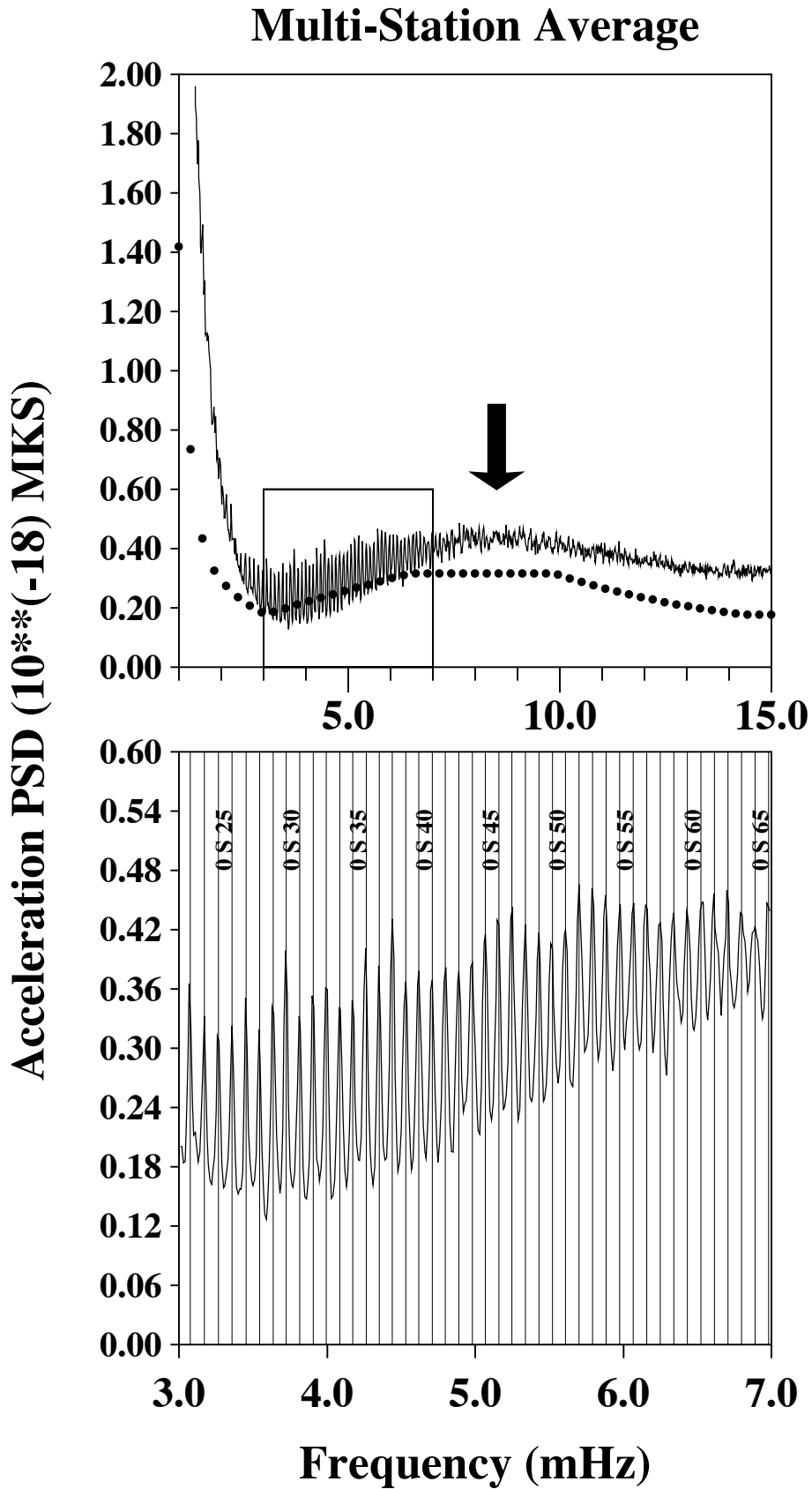


Figure 2

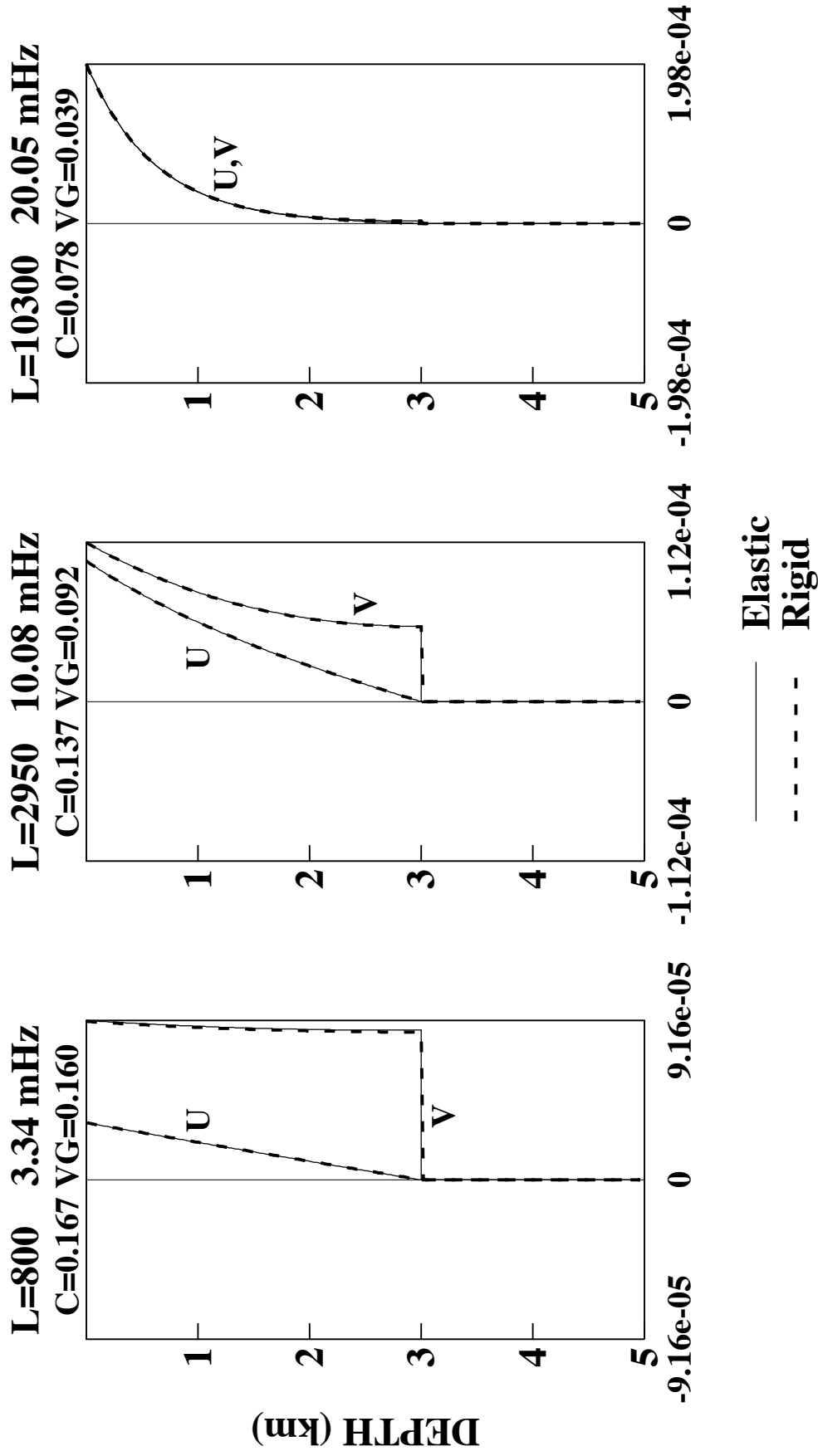


Figure 3

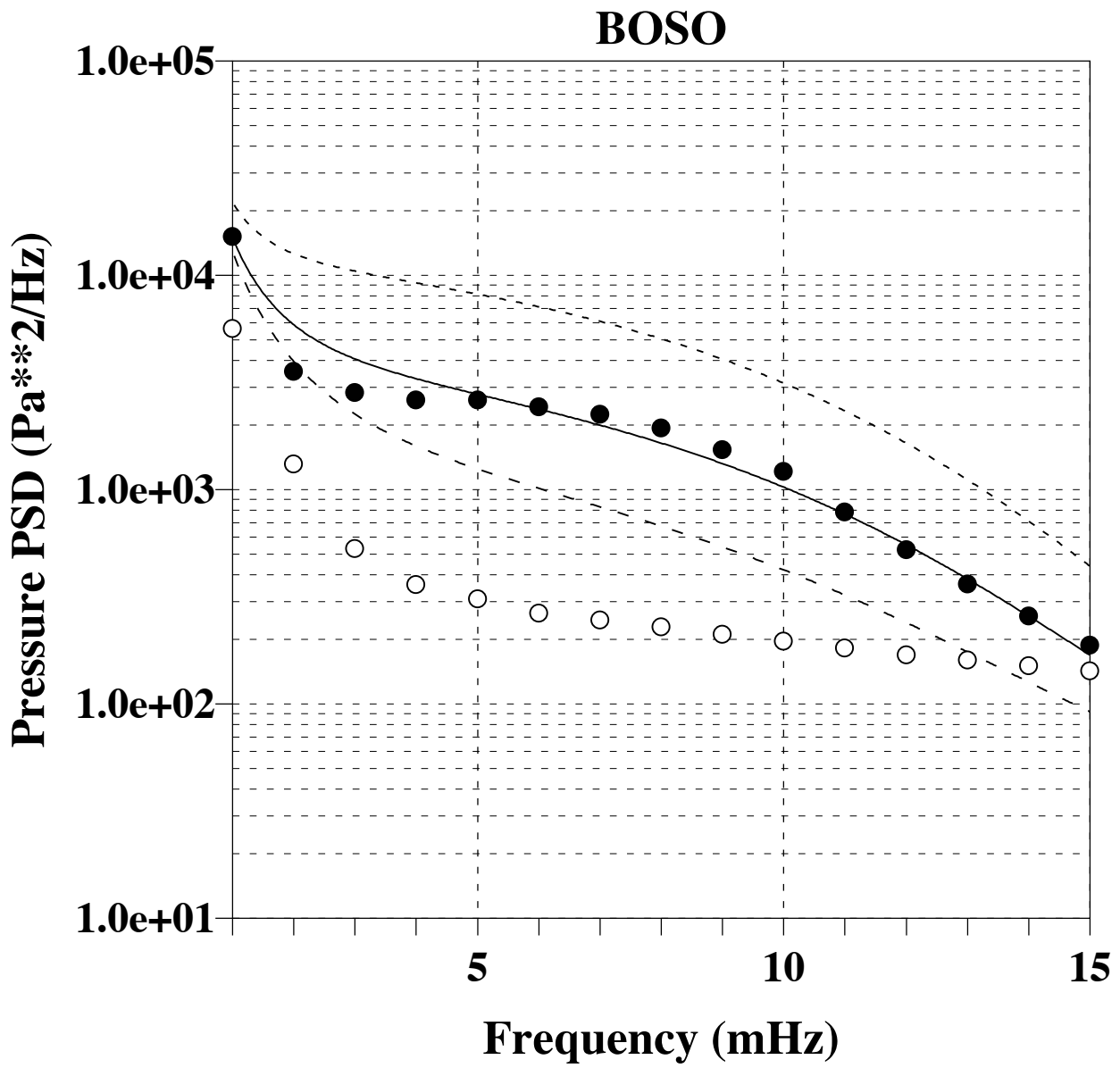


Figure 4

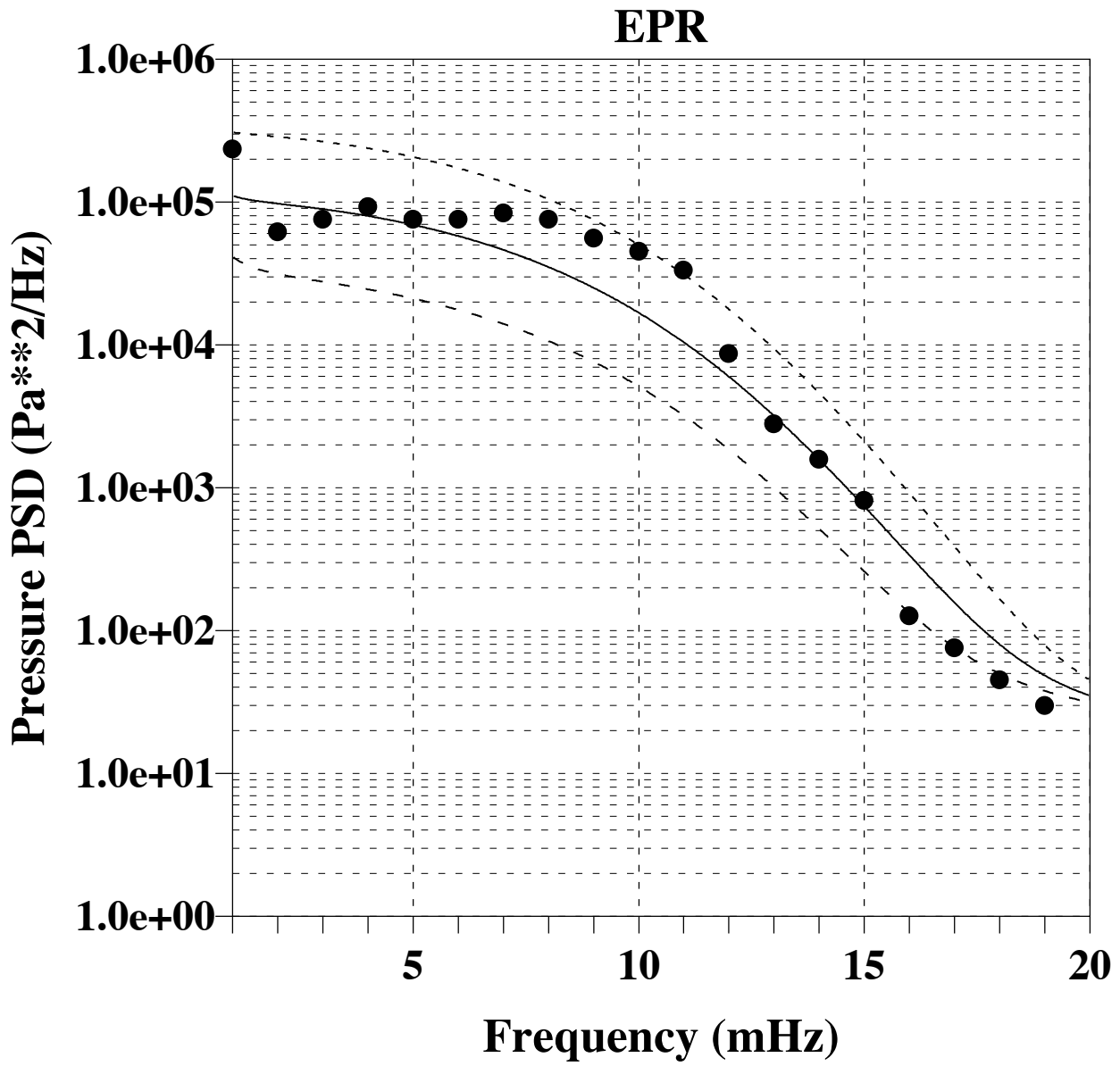


Figure 5

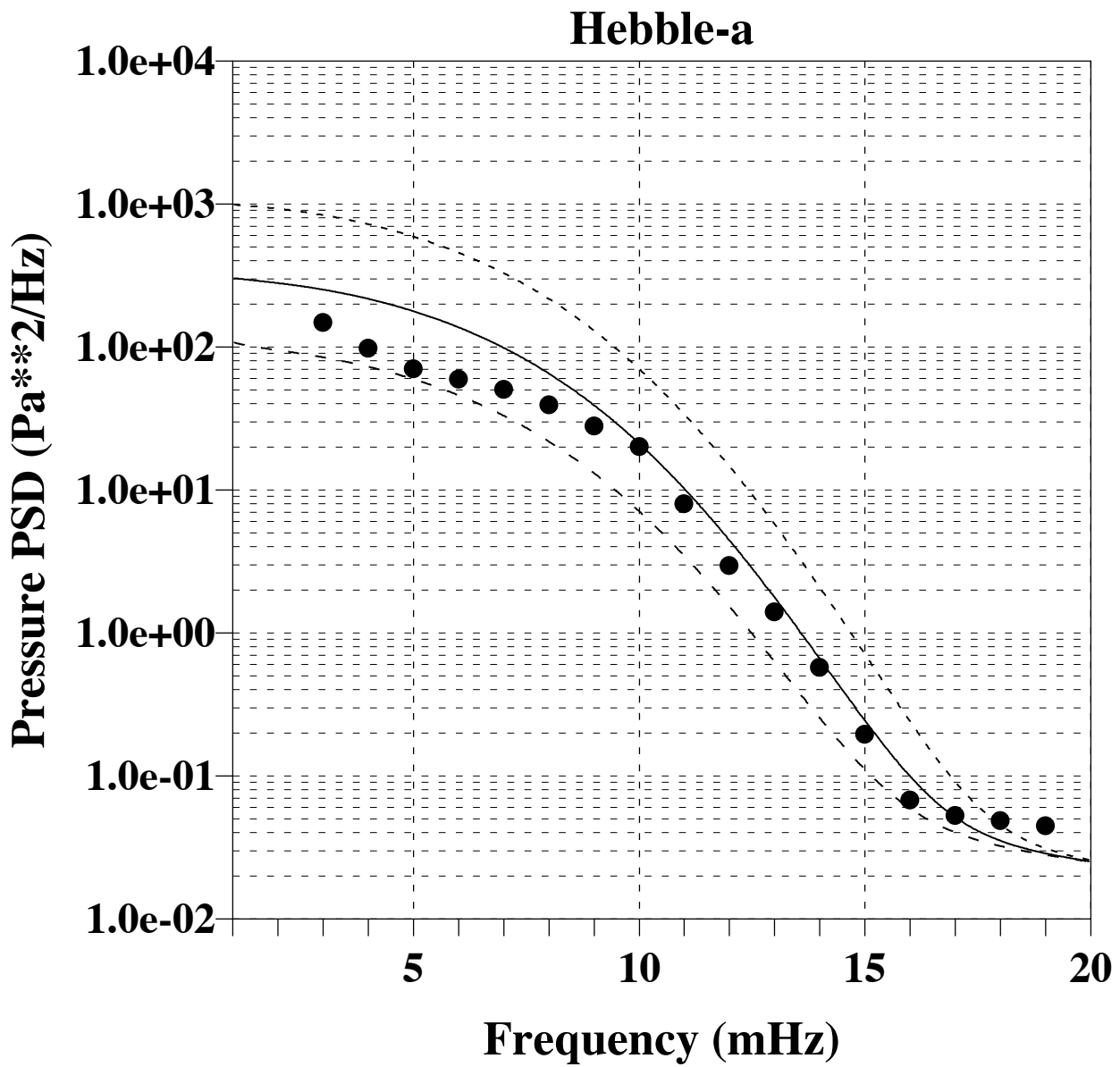


Figure 6

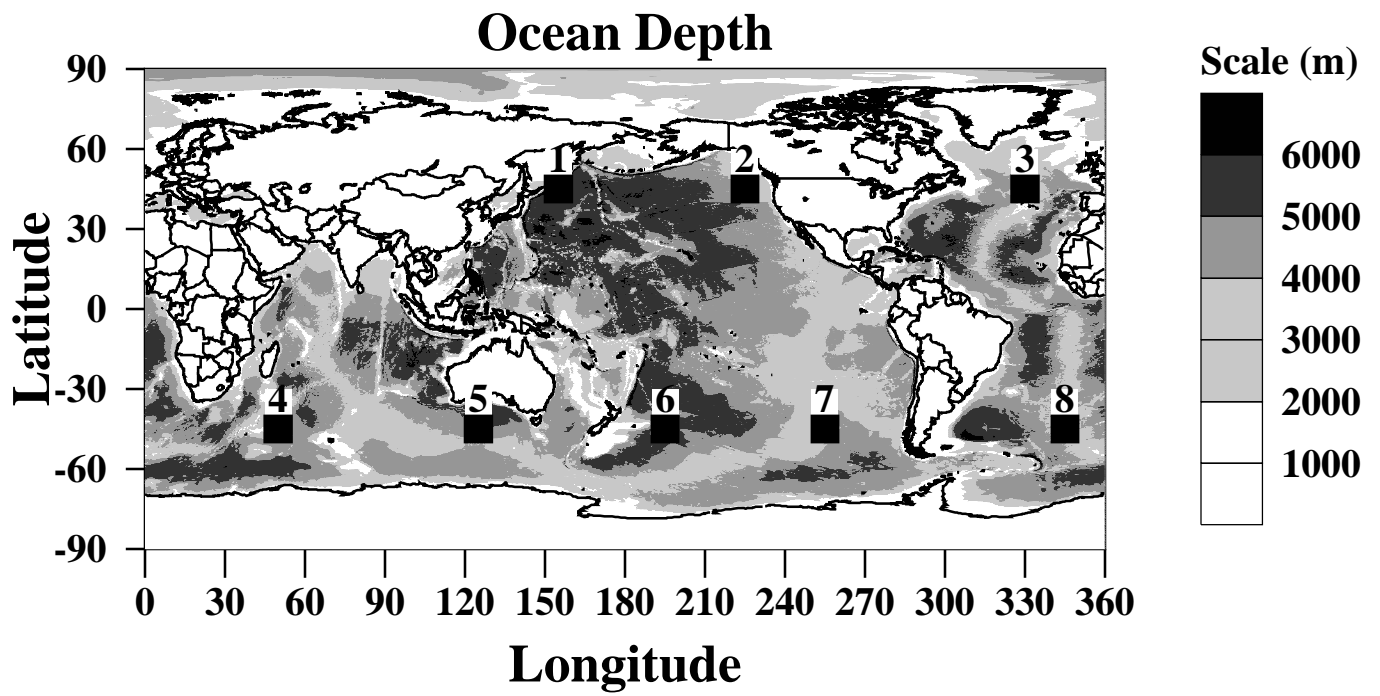


Figure 7

Acceleration PSD (m^{**2}/s^{**3})

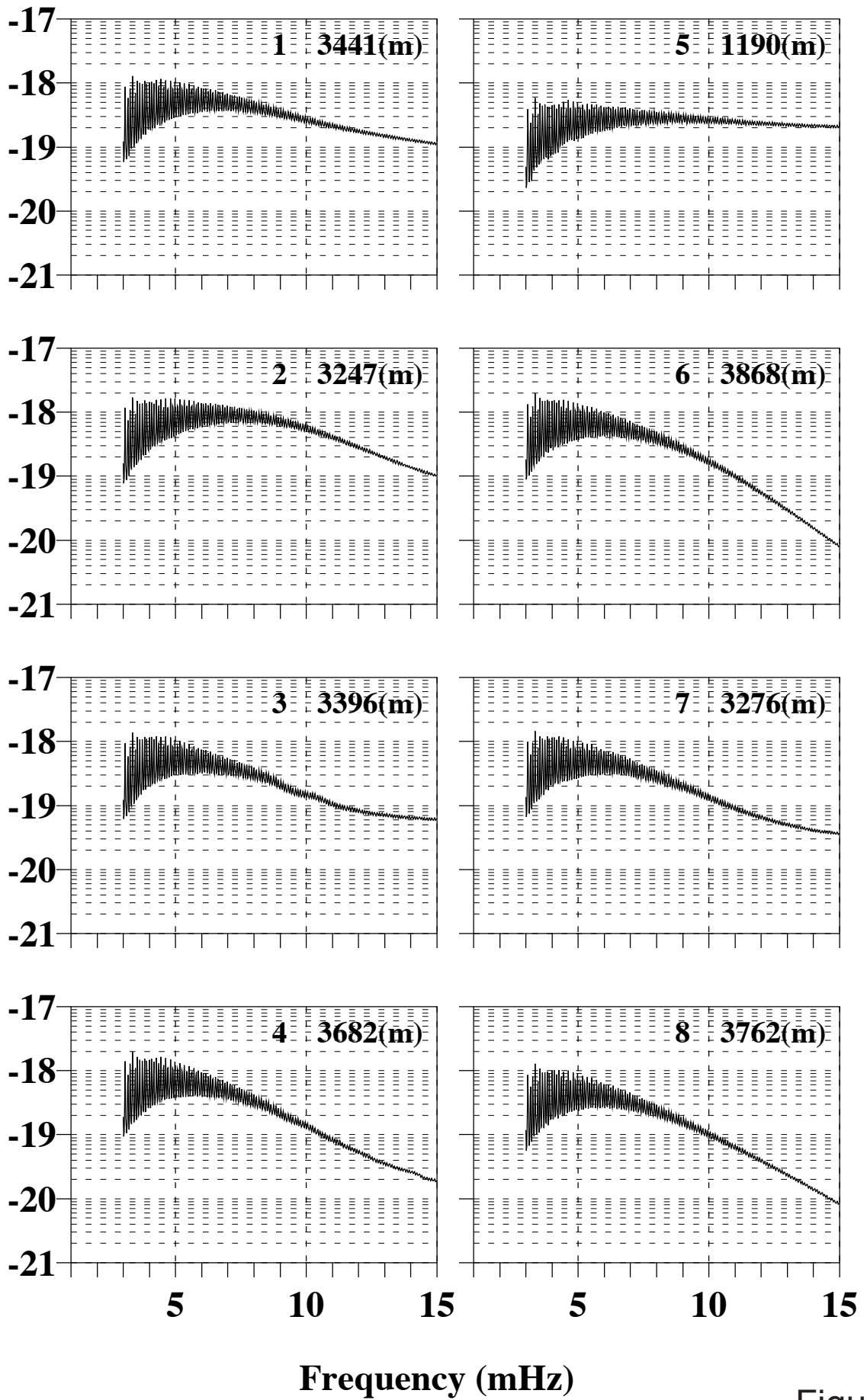


Figure 8

Effects of Ocean Depth

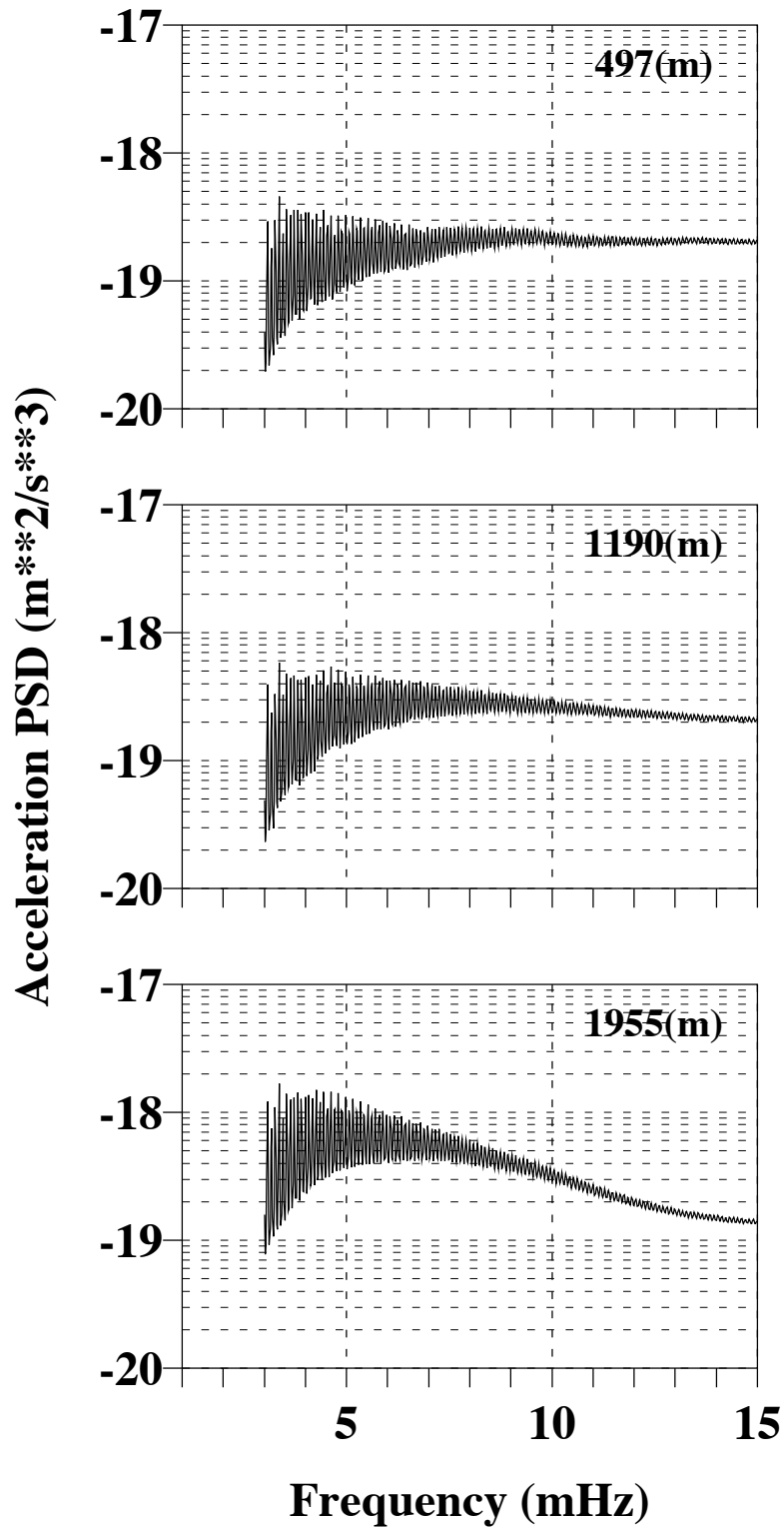


Figure 9

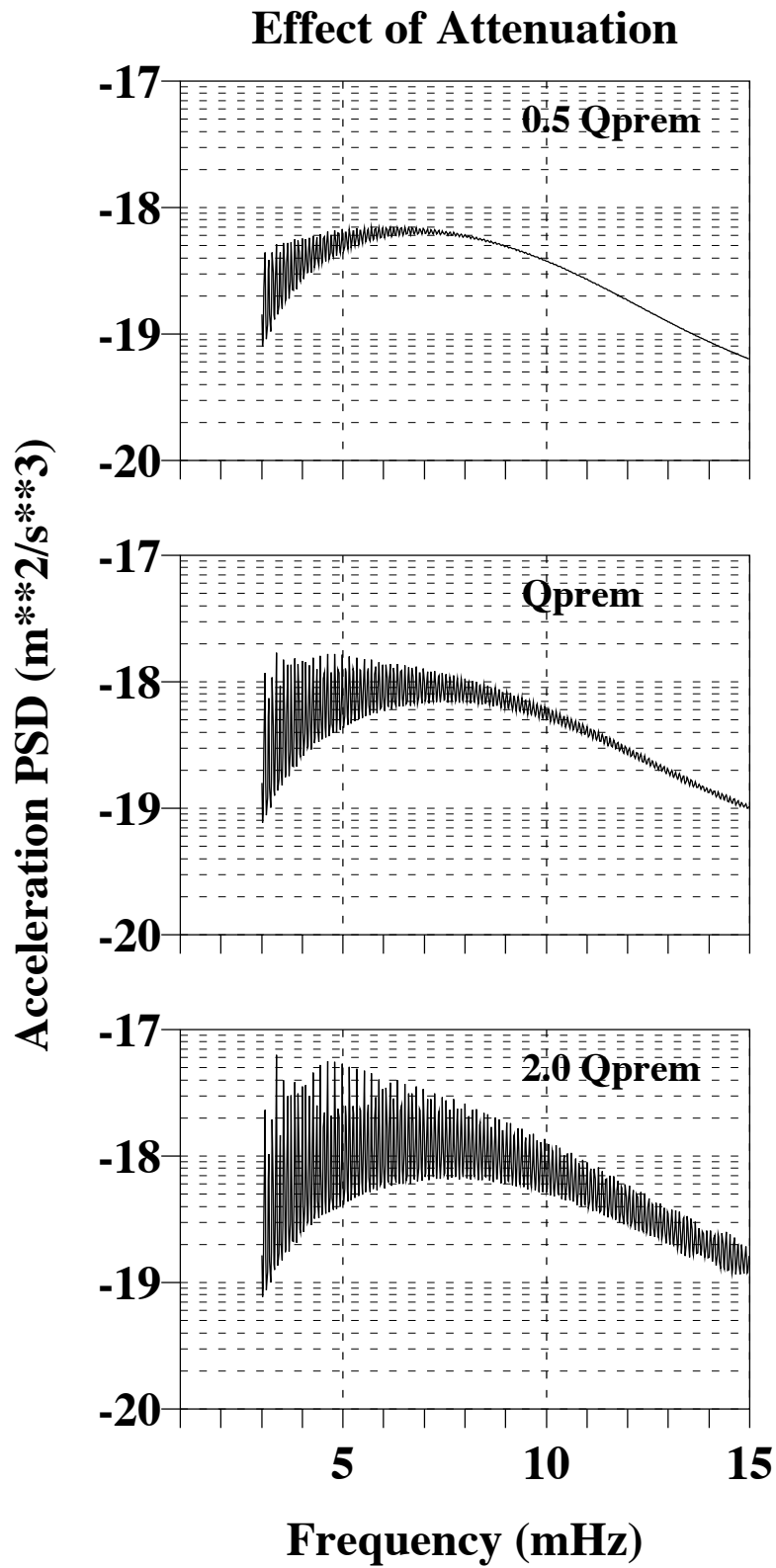


Figure 10

PAS

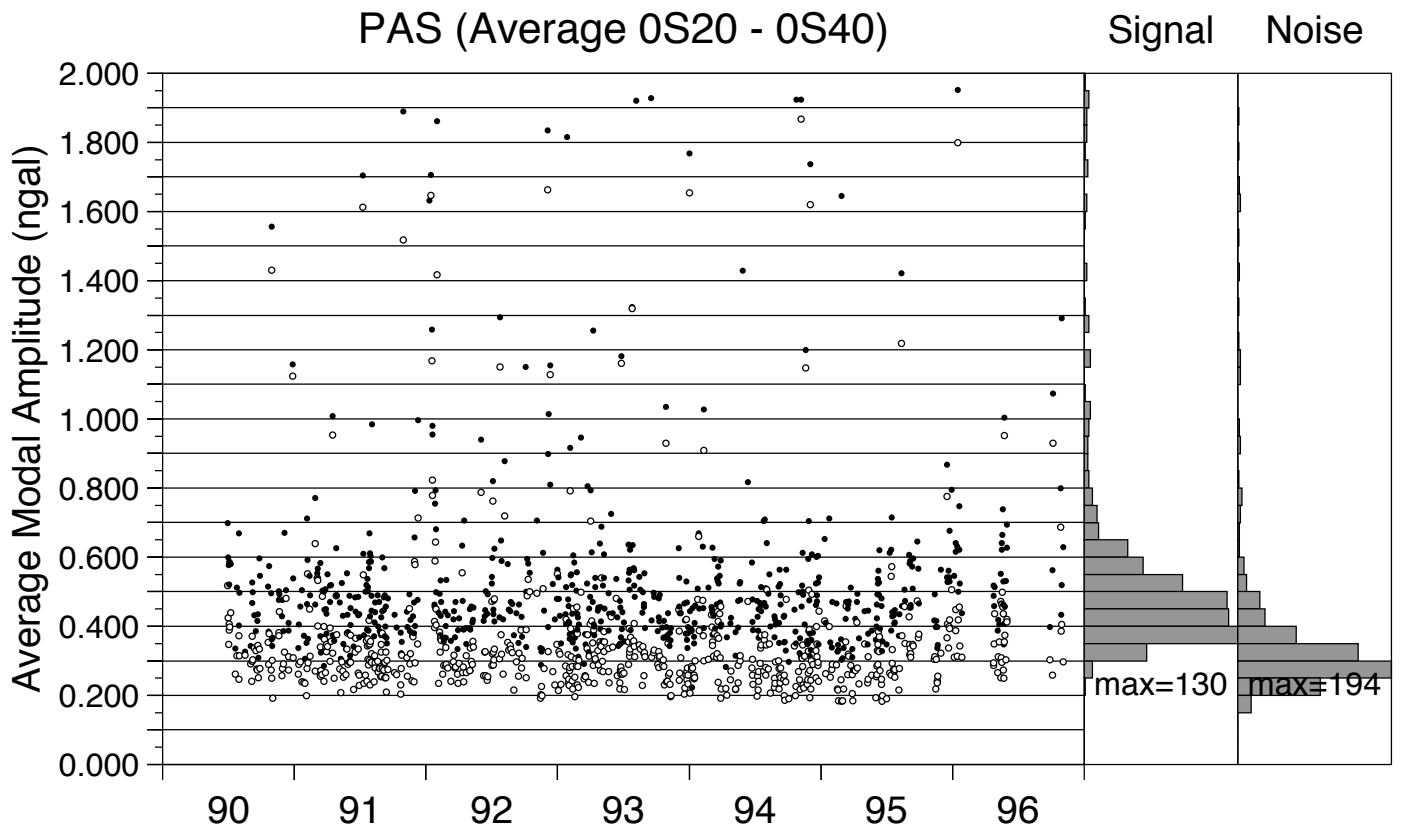
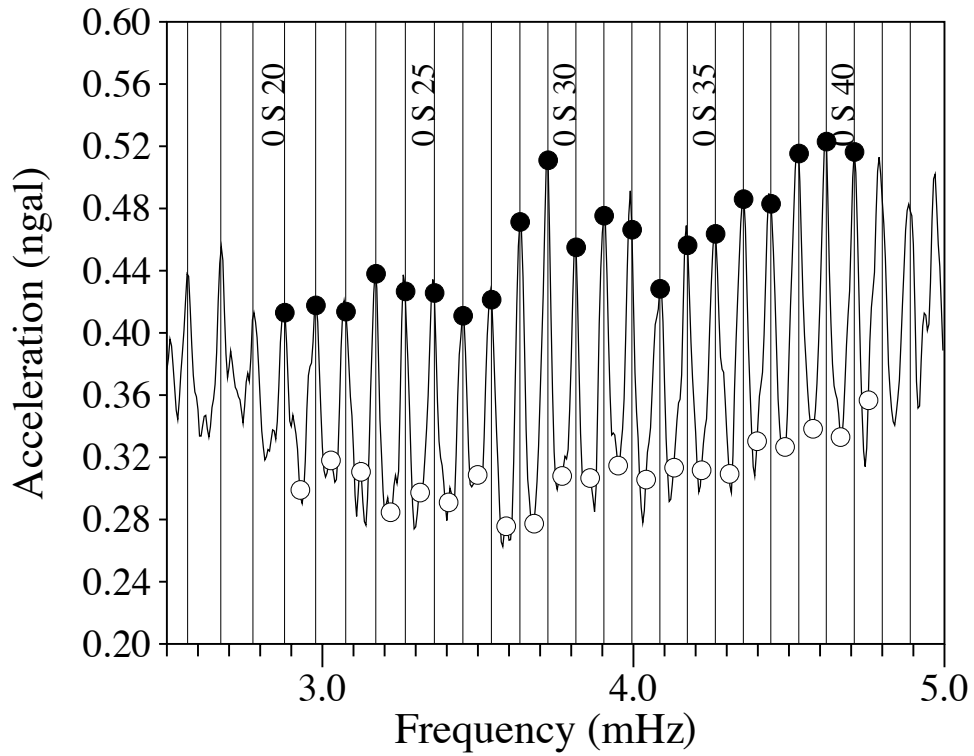


Figure 11

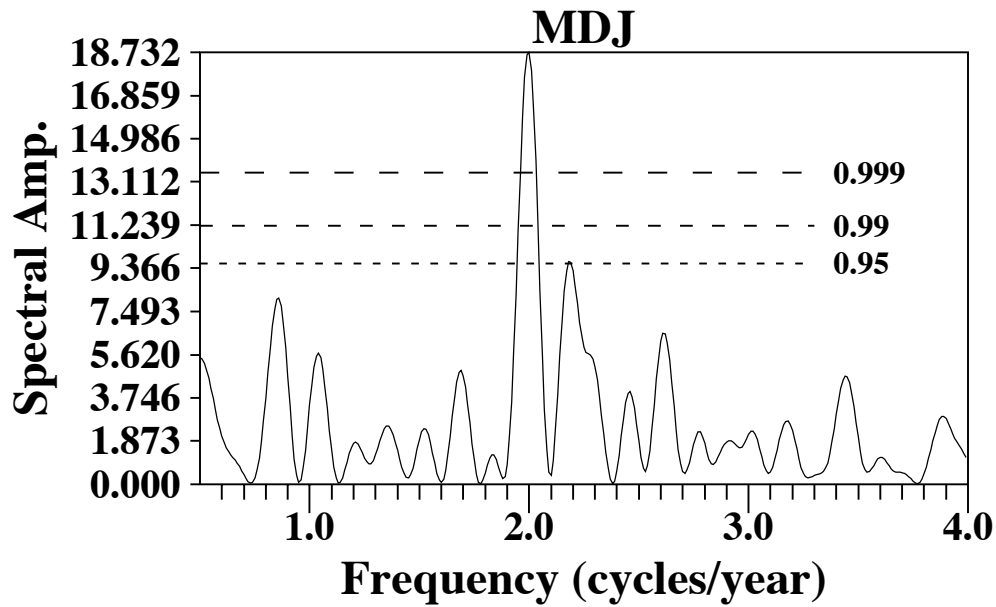
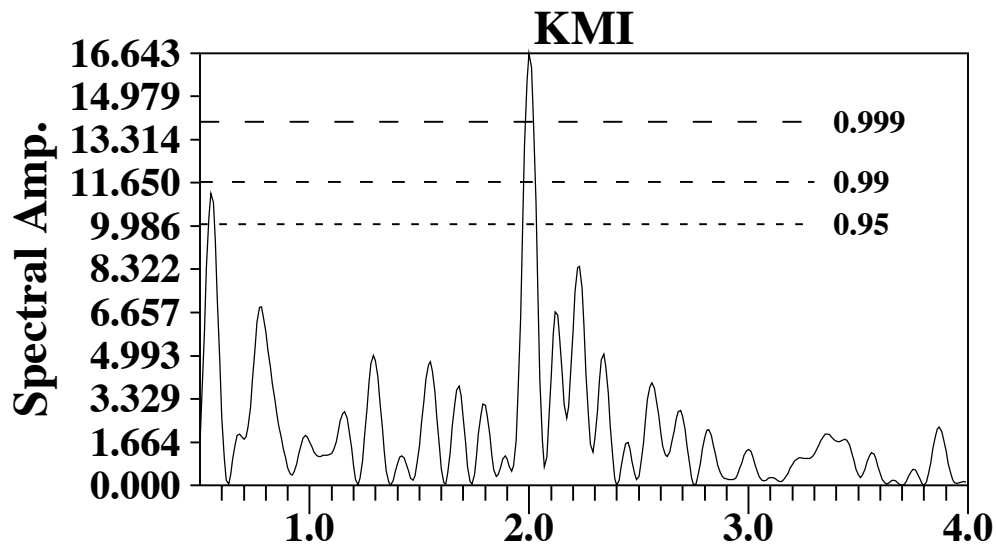
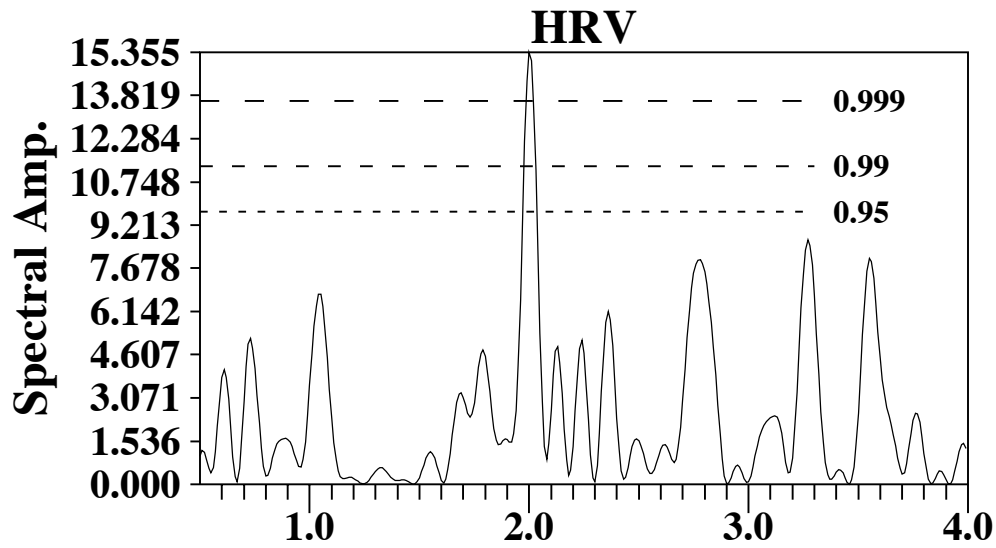


Figure 12

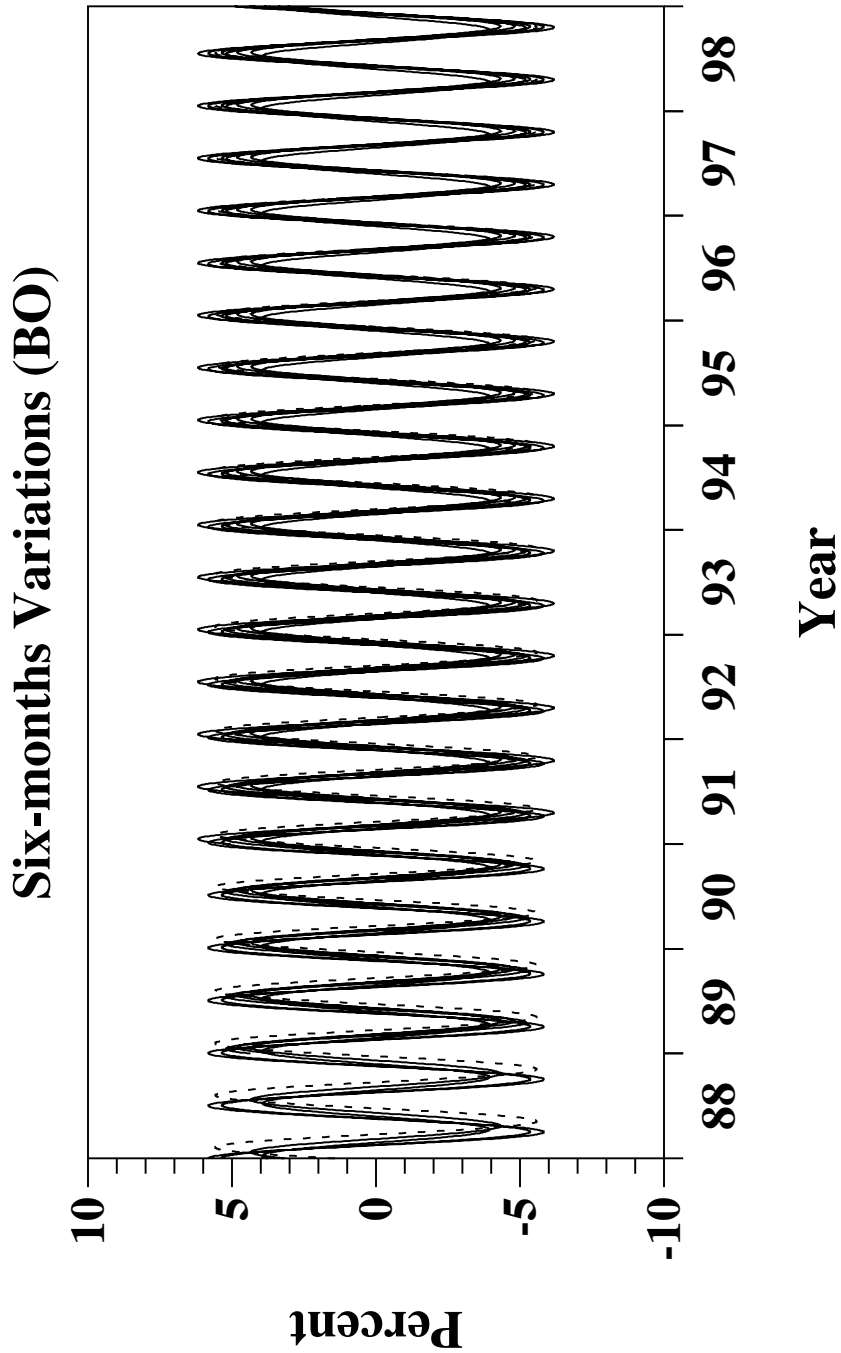
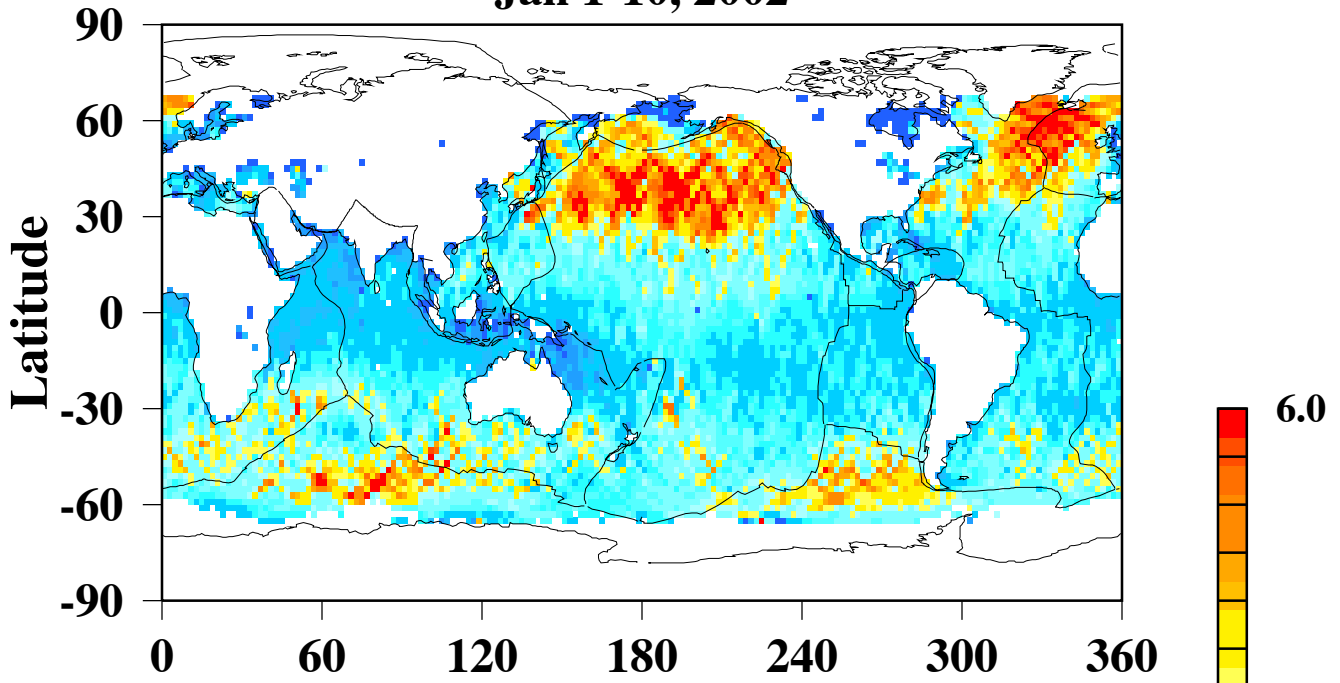


Figure 13

Significant Wave Height Jan 1-10, 2002



July 20-29, 2002

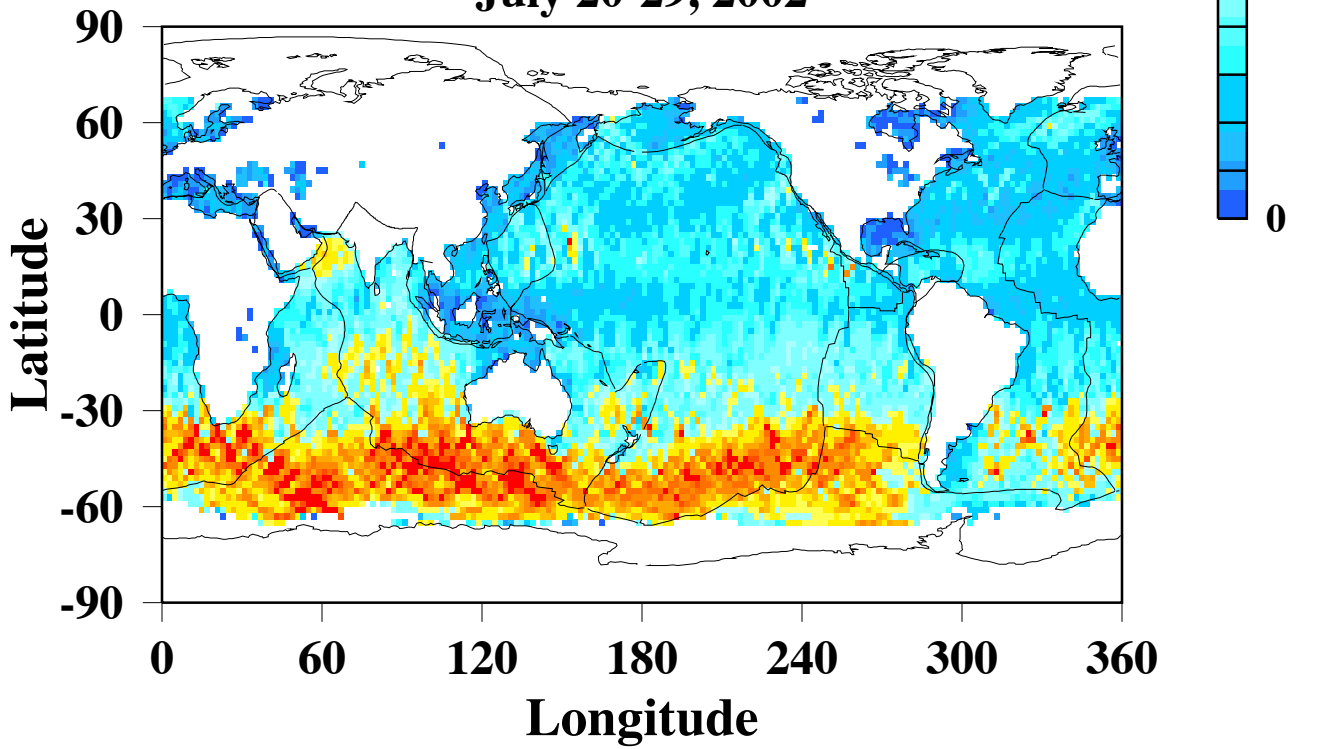


Figure 14

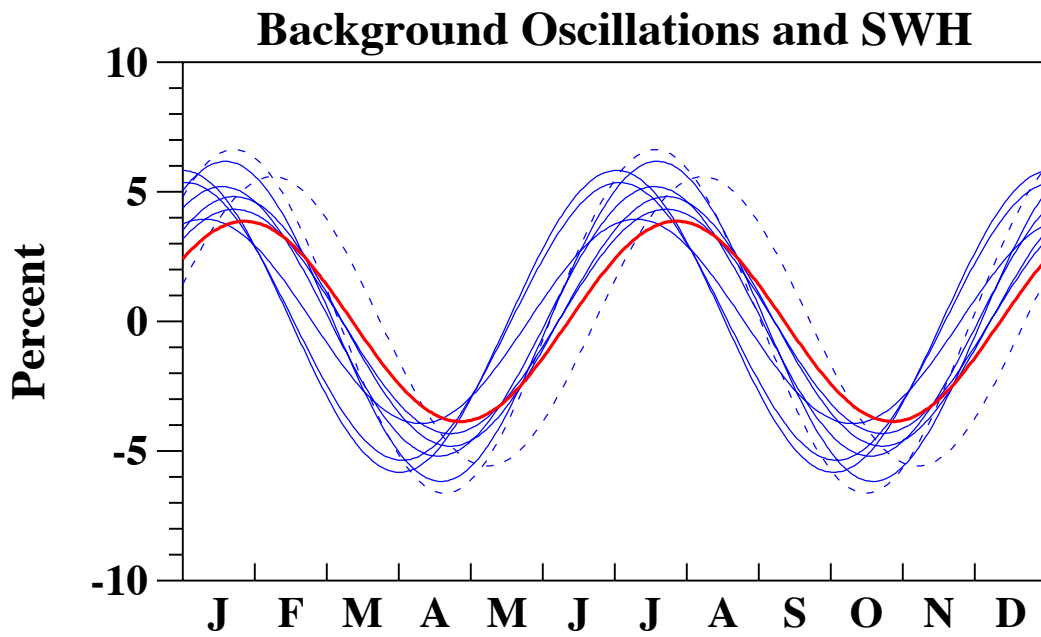
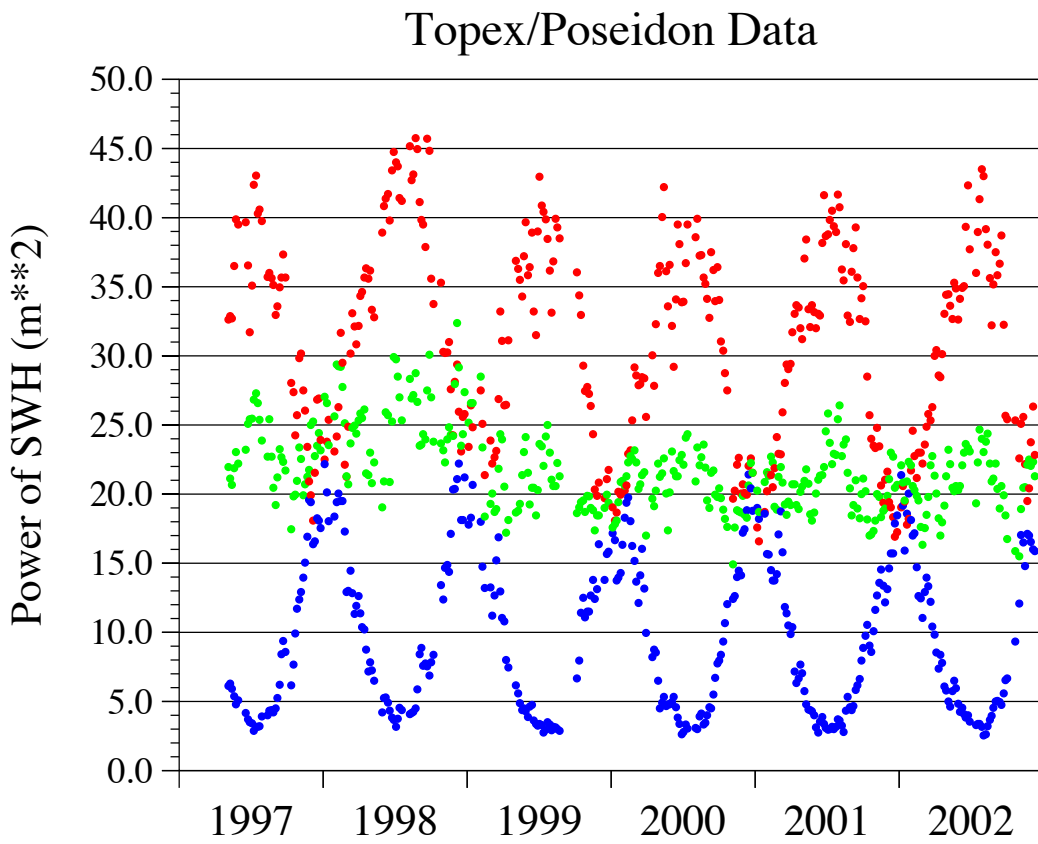


Figure 15